Synthesis, Antioxidant and Anti-In

flammatory Effects of Baicalin-Loaded Essen

tial Oil-Based Nano-Phytogel Ayurvedic Herbal Lip

http://knowledge.lancashire.ac.uk/id/eprint/5777

46/
doi.org/10.1007/s12668-025-0233

37-z

2006

Sutton, Ashish Dilip, Singh, Kama

linder and Shukla, Rahul (2026) Synergistic

Antioxidant and Anti-Inflammatory Effects

of Basic Lin-Loaded Essential Oil-Based Nano

-
P
h
y
t
o
g
e
l
.
B
i
o
N
a
n
o
S
c
i
e
n
c
e
,
1
6
.
I
S
S
N
2
1
9
1
-
1
6

30

Sue Ashish Dilip, Singh, Kamalinder

BioNanoScience (2026) 16:107
https://doi.org/10.1007/s12668-025-02337-z

RESEARCH

Synergistic Antioxidant and Anti-Inflammatory Effects of Baicalin-Loaded Essential Oil-Based Nano-Phytogel

Ashish Dilip Sutar[1] · **Kamalinder K. Singh**[2,3] · **Rahul Shukla**[1]

Received: 16 August 2025 / Accepted: 4 December 2025

Abstract

Baicalin (BA) is a potent flavonoid with antioxidant and anti-inflammatory properties; however, its clinical application is limited due to poor solubility and permeability. The present study aimed to develop an innovative baicalin-loaded essential oil-based lipid nanoparticle hydrogel (BA-NP-G) utilising rosemary oil (RO) as both an excipient and a therapeutic synergist for potential use in skin inflammatory disorders. BA-loaded lipid nanoparticles (BA-NPs) were formulated using a low-energy precipitation method. Following experimental optimisation for particle characteristics and encapsulation efficiency, nanoparticles were further embedded into a Carbopol-xanthan gum hydrogel. Characteristic results of BA-NPs, including size (174 ± 2.1 nm), PDI (0.25), ζ-potential (−30.01 mV), and high entrapment efficiency (up to 69.6 ± 1.1%), were confirmed. Antioxidant efficacy was assessed in vitro in RAW264.7 cells, while ex vivo skin permeation determined $C_{skinmax}$ and AUC. Stability was monitored for 90 days under multiple storage conditions, with the aim of predicting extended shelf life. Optimised BA-NP-G maintained chemical stability and >90% drug content for up to one year at 4 °C. Ex vivo skin permeation studies revealed a ~3-fold increase in epidermal drug deposition and ~2.5-fold increase in total skin AUC in drug delivery for BA-NP-G when compared against BA solution, with notably higher $C_{skinmax}$ and AUC values. Cellular response studies and antioxidant assays demonstrated superior free-radical scavenging activity when BA was encapsulated in NPs using RO as the liquid lipid, confirming a robust synergistic effect that markedly exceeded the activity of individual components. The BA-NP-G developed here combines the properties of both BA and RO, forming a synergistic blend within a nano-phytogel matrix to achieve significantly improved physical stability, enhanced skin bioavailability, and increased biological efficacy.

✉ Kamalinder K. Singh
KSingh1@lancashire.ac.uk

✉ Rahul Shukla
rahul.shukla@niperraebareli.edu.in;
rahulshuklapharm@gmail.com

[1] Department of Pharmaceutics, National Institute of Pharmaceutical Education and Research (NIPER-Raebareli), Bijnor- Sisendi Road, Sarojini Nagar, Near CRPF Base Camp, Lucknow, UP 226002, India

[2] School of Pharmacy and Biomedical Sciences, University of Lancashire, Preston PR1 2HE, UK

[3] Biomedical Evidence-based Transdisciplinary (BEST) Health Research Institute, University of Lancashire, Preston PR1 2HE, UK

Published online: 16 January 2026

Graphical Abstract

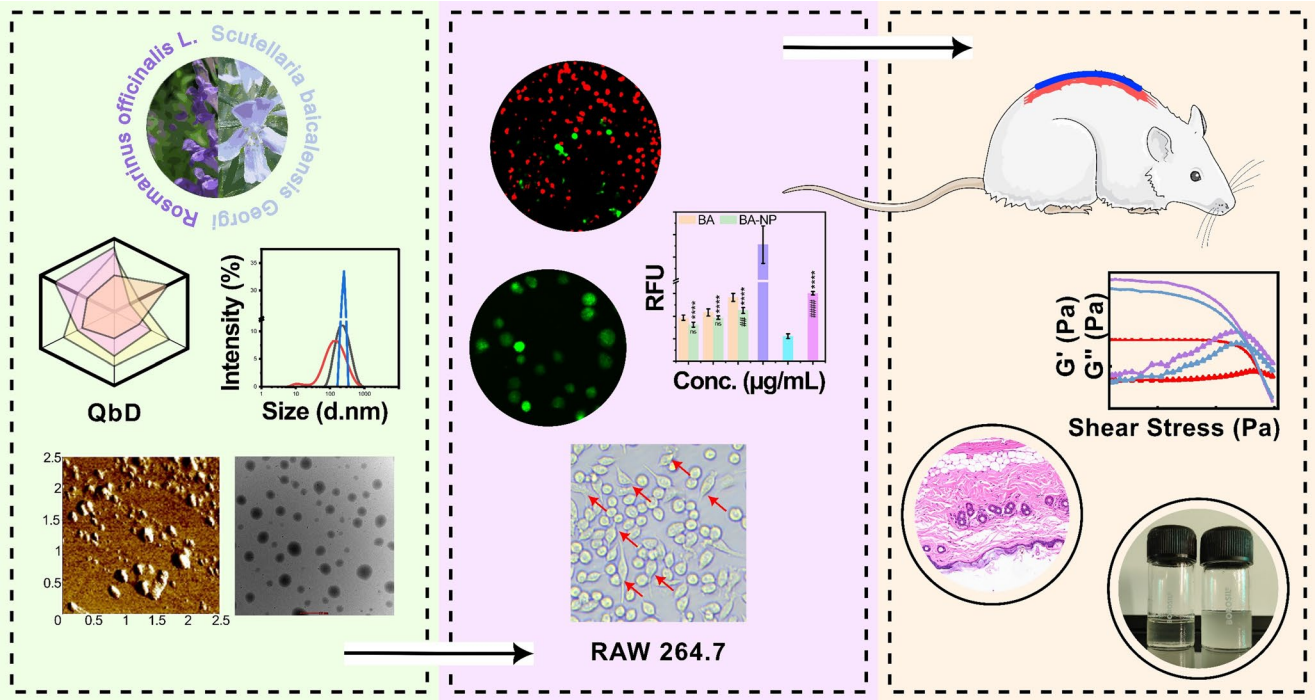

Keywords Baicalin · Rosemary oil · Nano-phytogel · RAW264.7 · Psoriasis

1 Introduction

Autoimmune skin condition "Psoriasis" is identified by hyperkeratinisation, thickening of epidermis, and immune cells in the dermis layer [1–3]. The complex pathogenesis of psoriasis involves the upregulation of pro-inflammatory cytokines, as shown in Fig. 1a, and elevated oxidative stress [4, 5]. Traditional therapies, including topical corticosteroids and calcineurin inhibitors, often result in local adverse effects such as irritation and barrier disruption. Systemic agents like methotrexate, although effective, are associated with serious risks, including immunosuppression and hepatotoxicity [6]. Treatment resistance, high cost, organ damage, discomfort, carcinogenic potential, and widespread immunosuppression limit the use of these medications [7, 8]. Hence, there is a need to explore novel formulations that have good efficacy with fewer side effects.

Baicalin (BA) is a flavone glycoside classified as a polyphenolic flavonoid, primarily isolated from *Scutellaria baicalensis* (Roots of Chinese skullcap) [9]. Baicalin showed both anti-inflammatory and antioxidant effects through various mechanisms: inhibition of the nuclear factor kappa-light-chain-enhancer of activated B cells (NF-κB) signalling pathway and activation of the nuclear factor erythroid 2–related factor 2 (Nrf2) antioxidant defence system via further suppression of cytokine release (Fig. 1a) [10–12]. These properties enable BA to minimise oxidative damage and suppress the production of inflammatory mediators, making it a promising therapeutic candidate for inflammatory skin disorders. However, its poor aqueous solubility, low membrane permeability, and chemical instability limit its bioavailability (~ 2–6%) [12–15].

Several studies have reported that BA-loaded nanocarriers, such as liposomes, nanostructured lipid carriers, and polymeric nanoparticles, show reduced systemic toxicity with enhanced anti-psoriatic activity [16–18]. These studies confirm BA's ability to modulate oxidative stress pathways. But most of these systems rely on synthetic excipients without exploring the therapeutic potential of natural essential oils. To explore this, natural essential oils are examined as functional excipients in a nanocarrier to prepare a dual-functional delivery platform. Rosemary oil (RO), from *Rosmarinus officinalis* L., is a mixture of monoterpenes and phenolic diterpenes such as 1,8-cineole, α-pinene, and carnosic acid [19–21]. They possess intrinsic antioxidant and anti-inflammatory activity. RO due to these active moieties exert synergistic therapeutic effects

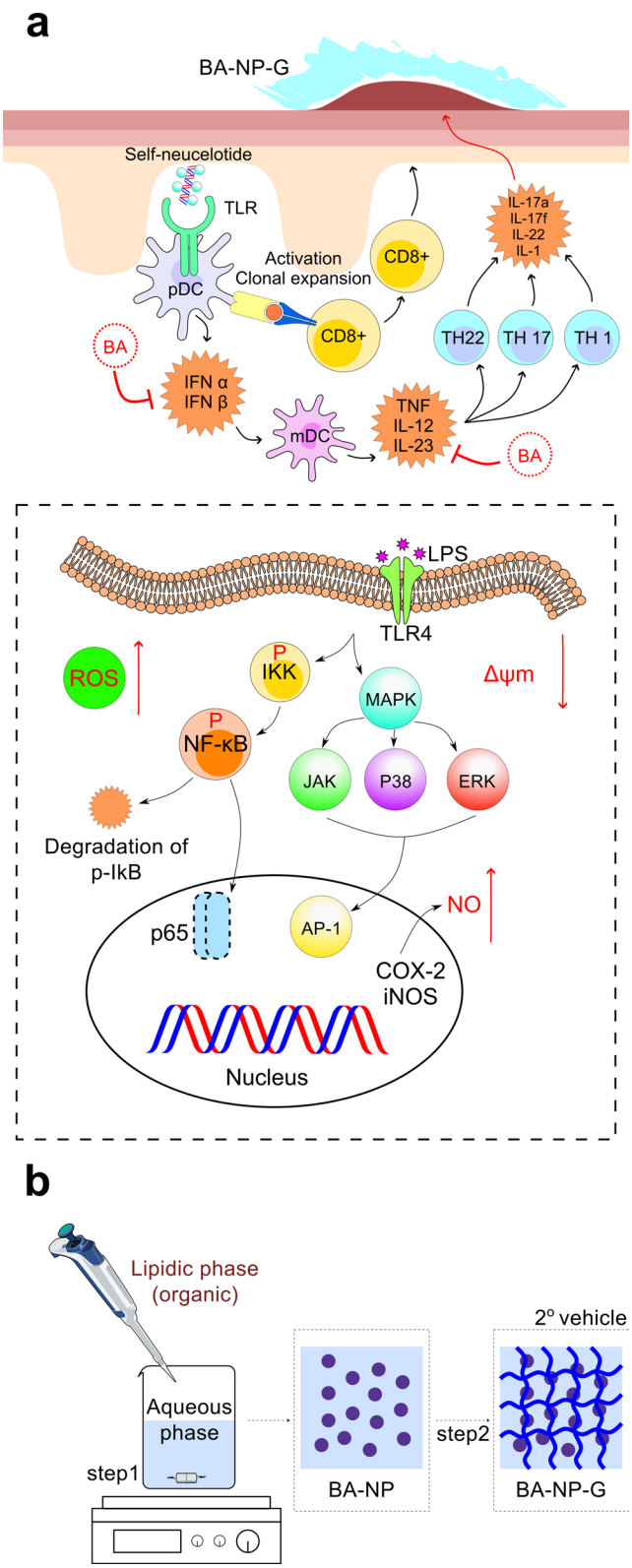

Fig. 1 (**a**) Proposed therapeutic mechanism showing immune response modulation by BA via inhibition of TLR-mediated activation, interferon production, T-cell responses, and inflammatory cytokine signalling. The dotted lower panel shows intracellular effects in LPS-activated macrophages, like antioxidant response, mitochondrial stabilisation, and inhibition of inflammation (**b**) BA-NP-G formulation process scheme

by scavenging reactive oxygen species and inhibiting pro-inflammatory pathways.

The present investigation explores the encapsulation of BA into an essential oil-based nanocarrier using RO as a lipidic excipient, thereby forming a BA-loaded lipidic nanoparticulate system. To facilitate topical application and improve local drug retention, this nanocarrier was further embedded into a Carbopol and xanthan gum-based hydrogel to formulate a nano-phytogel. The resulting BA-NP-G was further evaluated for its physicochemical properties, dermatokinetic properties, and biological efficacy, including cytocompatibility, anti-inflammatory potential, and modulation of oxidative stress.

2 Materials and Methods

2.1 Materials

Baicalin and rosemary oil were purchased from Sigma-Aldrich (St. Louis, MO, USA). Lipoid-S-75 was gifted by Lipoid GmbH (Ludwigshafen, Germany), and various excipients, including Tween-80, Carbopol 934, Xanthan gum, triethanolamine, and Bovine serum albumin (BSA), were obtained from Sisco Research Laboratory (Mumbai, India). Dulbecco's modified Eagle's medium (DMEM), Fetal bovine serum (FBS) from Gibco (Grand Island, NY, USA) and dichlorodihydrofluorescein diacetate (DCFDA), 3-(4,5-dimethylthiazol-2-yl)−2,5-diphenyltetrazolium bromide (MTT), 5,5′,6,6′-tetrachloro-1,1′,3,3′-tetraethyl-benzimidazolocarbo-cyanine iodide (JC-1), Lipopolysaccharide (LPS), etc., were procured from Hi-Media Laboratories Pvt. Ltd. (Mumbai, India). The organic solvents used are of HPLC grade, and the entire formulation procedure was carried out with triple-distilled Milli-Q water.

2.2 Drug Quantification and Analytical Confirmation

BA was dissolved in carbinol to prepare a stock solution, which was further diluted to obtain concentrations ranging from 2 to 10 µg/mL to find wavelength maxima (λ_{max}) using a UV-Visible spectrophotometer (Cary 60, Agilent Technologies, Santa Clara, CA, USA). The UV analysis method was used for drug analysis and drug release studies. In addition, a high-performance liquid chromatography (HPLC) method was developed to support analytical quantification, and this method was employed for quantifying drug retention in the skin layers (Chromatographic conditions– Agilent C18 column (250 mm × 4.6 µm), isocratic elution with 45% Milli-Q water containing 0.2% ortho-phosphoric acid and 55% methanol, at a flow rate of 1.2 mL/min, and detector set on 277 nm) [22].

2.3 Evaluation of Antioxidant Activity

The antioxidant activity of RO and BA was examined using the 2,2-diphenyl-1-picrylhydrazyl (DPPH) assay (0.039 mg/mL in methanol, equivalent to 0.1 mM), with ascorbic acid used as a reference. All samples were seeded in triplicate. Absorbance was measured at 517 nm following incubation in the dark. The percentage of radical scavenging activity was calculated. The methodology was adapted from our recent publication [23, 24].

2.4 Baicalin-Loaded Lipid Nanoparticle Design

Baicalin-loaded lipid nanoparticles (BA-NPs) were prepared using a low-energy precipitation technique (Fig. 1-b Step 1) [25]. Different ratios of Lipoid-S-75 and rosemary oil were used as the lipid phase, dissolved in 1 mL of ethanol. Baicalin (20 mg) was incorporated into this lipidic mixture. Tween 80 was dissolved in 20 mL of Milli-Q water in a separate beaker to serve as the aqueous phase. The lipidic phase was then introduced dropwise into the aqueous solution under continuous stirring at 1200 rpm until the ethanol had completely evaporated, facilitating emulsification.

The BA-NPs were optimised using a Quality by Design (QbD) approach, employing Box-Behnken Design (BBD), following ICH Q8 and Q9 guidelines. The process, including Quality Target Product Profile (QTPP) definition, identification of Critical Quality Attributes (CQAs), Critical Material Attributes (CMAs), and Critical Process Parameters (CPPs), was adapted from our previous work [23, 26], where particle size and encapsulation efficiency were prioritised as key attributes.

2.5 Characterisation of BA-NPs

2.5.1 Particle Size, Homogeneity, and ζ-Potential

The particle size (PS), ζ-potential and polydispersity index (PDI) of BA-NPs were examined using Malvern Zetasizer (Nano ZS, Malvern Zetasizer, United Kingdom). The NPs were diluted 10 times for PS measurement in a PS-specific cuvette, and the undiluted samples were checked for zeta potential [27].

2.5.2 Drug Loading and Entrapment Efficiency

To determine the entrapment efficiency (%EE), the BA-NP suspension was centrifuged at 9500 rpm for 60 min at 4 °C. The resulting supernatant was collected and analysed using UV–visible spectrophotometry. For drug loading (%DL), a known quantity of lyophilised BA-NP powder was dissolved in carbinol, and the BA concentration was quantified spectrophotometrically. The percentage of drug loading (Eq. 2) and entrapment efficiency (Eq. 1) were subsequently calculated [28].

$$\%EE = [W \cdot t \cdot -W \cdot f] \div W \cdot t \cdot \times 100 \quad (1)$$

$$\%DL = [W.t. - W.f.] \div [W.t. - W.f. + W.tl.] \times 100 \quad (2)$$

Whereas, W.t. = Total initial drug concentration, W.f. = Free drug concentration, and W.tl. = Weight of total lipid.

2.5.3 Morphological Analysis

The surface characteristics of BA-NPs were investigated using Transmission Electron Microscopy (TEM) and Atomic Force Microscopy (AFM). For TEM (JEM-2100, JEOL Ltd., Tokyo, Japan), the suspension was first diluted, then placed onto a copper grid coated with carbon film. After drying in a desiccator, images were captured to observe particle morphology. AFM analysis (NX12, Park Systems, Korea) was carried out in non-contact mode. Samples were dispersed in Milli-Q water, dried in a desiccator to preserve structural integrity, and scanned at a rate of 0.5 Hz to obtain surface topography [29].

2.5.4 Fourier Transform Infrared (FTIR) Spectroscopy

Attenuated Total Reflectance–Fourier Transform Infrared (ATR-FTIR) spectroscopy (Waltham, Massachusetts, USA) was utilised to record spectra within the range of 4000 to 600 cm^{-1}. This technique was employed to assess the compatibility between the drug, excipients, and the final formulation by identifying any shifts or changes in characteristic absorption bands, which may indicate molecular interactions or chemical modifications [23, 30].

2.5.5 Powder X-ray Diffraction Study

Raw BA and lyophilised BA-NPs were analysed using an X-ray diffractometer (XRD, Brucker AXS-D8 advance®, Karlsruhe, Germany) for their crystal behaviour. Diffractograms were recorded in a scanning range from 5 to 90° on a 2θ scale [31].

2.5.6 Drug Release Pattern Analysis

In vitro release of BA from BA-NPs was studied using the dialysis bag method (MWCO 12,000–14,000 Da; Himedia, India), with membranes pre-soaked in distilled water overnight. Samples containing free BA (firstly dissolved in ethanol

and further diluted with PBS) and BA-NPs (~ 5 mg BA) were placed in bags and incubated in 100 mL phosphate-buffered saline (pH 7.4 and 5.2) at 37 ± 0.5 °C with continuous stirring (50 rpm). Samples (1 mL) were taken at set intervals over 24 h and replaced with fresh buffer. Drug release was quantified by UV spectrophotometry and fitted into kinetic models via regression analysis (R^2 values) [32, 33].

2.6 Cell Line Studies

RAW 264.7 macrophages were cultured in DMEM containing 10% FBS and 1% penicillin-streptomycin at 37 °C with 5% CO_2. Bulk BA and lyophilised BA-NPs were dissolved in DMSO, filtered (0.25 µm), and diluted in serum-free medium for further experiments [34, 35].

2.6.1 Cell Viability Assay

Cell viability was assessed using the MTT assay according to the standard protocol. Briefly, cells were seeded in 96-well plates (10,000 cells/well) and incubated for 24 h, followed by treatment with various concentrations of BA and BA-NPs (100 µL/well) and further incubation for 24–48 h as required. After treatment, a MTT solution (5 mg/mL, 100 µL/well) was added and incubated for 3 h. The supernatant was then discarded, and the formazan crystals were solubilised using 100 µL DMSO. Absorbance was measured at 570 nm using a microplate reader (BioTek Synergy H1, Agilent, U.S.A.) [35, 36]. The same procedure was followed to assess cytotoxicity of the drug, formulation, and LPS, as well as the effect of drug and formulation treatment on cell viability in LPS-induced inflammatory cells.

2.6.2 Cellular Response Assays

Macrophage cells were used to evaluate cell differentiation, intracellular reactive oxygen species (ROS) accumulation [37], and nitric oxide (NO) production [38–40]. For differentiation analysis, healthy and LPS-stimulated cells were seeded in 24-well plates at a density of 2.5×10^5 cells/well for 24 h, after which morphological changes were seen using a microscope. To analyse ROS levels, cells were seeded in 6-well plates (1×10^6 cells/well) for 24 h and stimulated with LPS, and then stained with 10 µM DCFH-DA in SFM at 37 °C for 20 min in the dark. After washing with PBS, cells were treated with various concentrations of BA and BA-NPs for 2 h, followed by fluorescence imaging and quantification using ImageJ software. For NO estimation, LPS-stimulated cells were seeded in 24-well plates (2.5×10^5 cells/well), incubated for 24 h, and treated with BA or BA-NPs. After the treatment, 250 µL of Griess reagent was added, and the absorbance was measured at 540 nm to determine nitrite levels, which reflect NO production.

2.6.3 Mitochondrial Depolarisation Study

Mitochondrial membrane potential (Δψm) was analysed using JC-1 dye according to the standard protocol [41, 42]. Following treatment with BA, BA-NPs, or LPS, the cells were incubated with JC-1 staining solution for 10 min at 37 °C. After staining, cells were washed twice with buffer to remove excess dye. LPS was used as a positive control. Fluorescence images were captured using a fluorescence microscope and quantified using ImageJ software. Red aggregates and green monomers indicated changes in mitochondrial membrane potential.

2.7 Loading of BA-NPs into Gel Matrix

Hydrogels were prepared using Carbopol-934P at concentrations of 0.5%, 0.75%, and 1% w/v, in combination with constant 0.25% w/v xanthan gum (Fig. 1-Step 2) [43]. These polymers were dissolved in purified water under continuous stirring at 500 rpm for 5–6 h at ambient temperature (~ 25 °C) until a homogenous gel base was formed. The pH of the mixture was adjusted using triethanolamine to facilitate gelation. Once the base was stabilised, pre-synthesised BA-NPs (equivalent to 20 mg BA for 10 mL of gel) were gradually incorporated into the gel under constant agitation to achieve uniform distribution within the matrix.

2.8 Characterisation of BA-NP-Loaded Hydrogel

The resulting BA-NP hydrogels (BA-NP-G) were characterised to assess both their physicochemical and rheological properties. Rheological studies were performed using an advanced rheometer (MCR 302, Anton Paar GmbH, Graz, Austria) at 25 °C, evaluating parameters such as storage modulus (G'), loss modulus (G''), amplitude and frequency sweep, as well as shear stress–strain and viscosity behaviour [44–47]. The performance of the prepared gels was benchmarked against a commercially available anti-psoriatic hydrogel (MF). The physical evaluation included appearance, spreadability, and washability, which were tested by applying the gel to the dorsal hand skin and then rinsing it with water. The pH was determined by diluting 5 g of gel with 20 mL of warm water, with measurements recorded in triplicate. For uniformity of drug content, 1 mL of gel was dispersed in 10 mL of water, and samples were collected from three vertical positions (top, middle, and bottom) within the container. Drug content was quantified using UV spectrophotometry to ensure homogeneity.

2.9 Ex Vivo Skin Permeation Study

The permeation of the formulation was examined using Franz diffusion cells and hairless abdominal skin of Balb/c mice, as previously described in our earlier work [23, 30]. Hairless mouse abdominal skin was used as an ex vivo model due to its comparable barrier function and lipid composition to human skin, providing predictive correlation for human transdermal permeation [48, 49]. Briefly, the receiver compartment was filled with PBS (pH 7.4) at 37 ± 0.5 °C. The donor compartment was loaded with BA-NP-G (equivalent to 2 mg BA), and samples were taken at regular intervals up to 8 h. Cumulative drug permeation, flux (J), and permeability coefficient (Kp) were calculated using standard equations.

2.10 Ex vivo Dermatokinetic Study

A dermatokinetic study was conducted following the same parameters as an ex vivo permeation experiment to assess drug distribution across different skin layers [50–53]. BA dispersion and BA-NP-G were seeded in the donor compartment of the BALB/c mice skin-mounted Franz diffusion cells. At predetermined time points, the skin sections were collected, gently rinsed with saline (pH 7.4), and immersed in hot water (2–4 min) to remove any residual formulation. The epidermis and dermis were then carefully separated using forceps, finely chopped, and immersed in 2 mL of methanol for 24 h to extract the encapsulated BA. The amount of drug retained in each skin layer was subsequently quantified using HPLC.

2.11 Stability Studies

Stability studies of BA-NPs and BA-NP-G were conducted over period of three months, following ICH guidelines, to monitor changes in the active component and physical characteristics under different environmental conditions [54–56]. Samples were stored at 4 ± 1 °C (refrigerated), 25 ± 2 °C/60 ± 5% RH (ambient), and 40 ± 2 °C/75 ± 5% RH (accelerated) for evaluation at 1, 2, and 3 months.

2.12 Statistical Analysis

Statistical analysis was performed using GraphPad Prism (GraphPad Software, San Diego, CA, USA). Following a significant effect examined by one-way or two-way analysis of variance (ANOVA), desirable multiple comparison tests were used to assess differences between group results. All tests were conducted at a significance level of $\alpha = 0.05$, with corrections for multiple testing based on the chosen procedure.

3 Results and Discussion

3.1 Assay Methods

UV-Visible spectrophotometry showed that the maximum absorbance (λ_{max}) for BA occurred near 277 nm (Fig. 3a). Based on this, a HPLC method was established for the quantification of BA. Analysis was carried out on a C18 column (250 mm × 4.6 µm) under isocratic elution using a mobile phase composed of 45% triple distilled water (TDW) containing 0.2% ortho-phosphoric acid and 55% methanol, at a flow rate of 1.2 mL/min. The detector was set on 277 nm, with BA eluting at retention time of approximately 4.5 min (Fig. 3b) within a total run time of 7 min. The injection volume was set to 10 µL, and the column temperature was maintained at 30 °C. This method provided reliable and selective quantification of BA.

3.2 Pre-Formulation Antioxidant Evaluation

As shown in Fig. 3e, BA and RO exhibited a concentration-dependent increase in % DPPH neutralisation. BA showed moderate antioxidant activity, while RO demonstrated a less pronounced but comparable effect. The antioxidant potential of RO may be due to its phenolic constituents, such as rosmarinic acid, carnosic acid, and carnosol, which are well-known for their radical scavenging activity [19, 20]. These findings supported the use of RO in further formulation of BA-NPs, with the goal of enhancing antioxidant efficacy through potential synergistic interactions.

3.3 Optimisation of BA-NPs Using Box–Behnken Design

The BA-NP formulation was systematically optimised using a Quality by Design (QbD) approach in accordance with ICH Q8 guidelines, employing JMP statistical software (Version 18, SAS Institute Inc., Cary, NC, USA) for experimental design and data analysis. Preliminary studies and risk assessment identified total lipid content and Tween-80 concentration as CMAs, and sonication time as CPPs with significant influence on the CQAs, specifically PS and %EE. A BBD was employed to evaluate both individual and interactive effects of CMAs and CPP using response surface methodology. A total of 17 experimental runs were conducted (Table 1), yielding a wide variation in PS (110 to 542 nm) and %EE (41.21% to 69.64%).

The model fits the data from Table 2, demonstrating an excellent correlation and predictive capacity. The regression model for PS exhibited a coefficient of determination (R^2) of 0.921 and an adjusted R^2 of 0.819, with a low root mean

Table 1 Experimental design and results for BA-NPs development

	Components of BA-NPs				
	Independent variables and their levels				
Component	Unit	Low (−1)	Mid (0)	High (+1)	
Total lipid (X1)	mg	80	100	120	
Tween-80 (X2)	mg	60	80	100	
Sonication time (X3)	min	2	4	6	
	Dependent variables and their constraints				
Particle size (Y1)		nm	Minimized		
Encapsulation efficiency (Y2)		%	Maximized		
	Design space of BA-NPs using Box Behnken Design, limiting trials to 17 runs				
Run no.	X1	X2	X3	Y1	Y2
1.	120	80	6	288 ± 5.2	41.85 ± 1.2
2.	100	80	4	206 ± 3.6	69.64 ± 1.1
3.	120	100	4	139.9 ± 8.2	46 ± 2.1
4.	80	100	4	110.2 ± 4.6	44.97 ± 1.2
5.	100	80	4	206 ± 6.2	69.64 ± 1.1
6.	100	80	4	206 ± 6.2	69.64 ± 1.1
7.	100	60	6	252.1 ± 12.2	65.1 ± 1.2
8.	120	80	2	445.1 ± 8.23	41.21 ± 0.6
9.	100	80	4	206 ± 6.2	69.64 ± 1.1
10.	80	60	4	230 ± 12.5	41.23 ± 0.5
11.	80	80	6	154.1 ± 8.5	41.69 ± 0.5
12.	120	60	4	542 ± 7.5	45.97 ± 1.1
13.	100	80	4	206 ± 6.2	69.64 ± 1.1
14.	100	100	6	146.8 ± 4.6	43.23 ± 2.3
15.	100	100	2	199.9 ± 10	57 ± 2.1
16.	100	60	2	301.4 ± 15	45.87 ± 1.7
17.	80	80	2	242.6 ± 13	44.38 ± 1.3

All runs were conducted in triplicate ($n = 3$)

Table 2 Statistical model summary and optimal conditions for BA-NPs

Summary of fit						
Y1	R^2	Adjusted R^2	RMSE	MR		
Y2	0.9211	0.8197	46.25	240.12		
	0.9825	0.9600	2.47	53.33		
ANOVA						
Parameters	DF	SS	MS	F-ratio	*p*-value	Model significance
Y1						
Model	9	174940.20	19437.8	9.0844	0.0041	Significant
Error	7	14977.79	2139.7	-	-	-
C. total	16	189917.99	-	-	-	-
Y2						
Model	9	2415.21	268.3	43.68	0.0001	Significant
Error	7	43.00	6.1	-	-	-
C. total	16	2458.21	-	-	-	-
Optimal values, Desirability search approach						
Sample	X1	X2	X2	Y1	Y2	Desirability
BA-NPs	98.48	86.64	4.06	169.60	68.35	0.862518

square error (RMSE) of 46.3, indicating a well-fitting model. Similarly, the %EE model demonstrated an even stronger fit, with $R^2 = 0.983$ and adjusted $R^2 = 0.960$, accompanied by an RMSE of 2.48. The significance of the models was confirmed by ANOVA, with *p*-values well below 0.005 and high F-values (9.08 for PS and 43.68 for EE), indicating that the selected CMAs and CPP were the primary contributors to response variability.

The regression equations were derived as follows:

$$PS = 206 + 84.76X_1 - 91.08X_2 - 43.5X_3 - 70.57X_1X_2 - 17.15X_1X_3 - 0.95X_2X_3 + 53.46X_1^2 - 3.93X_2^2 + 22.98X_3^2 \quad (3)$$

$$\%EE = 69.64 + 0.345X_1 - 0.87X_2 + 0.426X_3 - 0.9275X_1X_2 + 0.8325X_1X_3 - 8.25X_2X_3 - 17.80X_1^2 - 7.29X_2^2 + 9.55X_3^2 \quad (4)$$

Where X_1 = Total lipid (mg), X_2 = Tween-80 (mg), and X_3 = Sonication time (min).

The actual vs. predicted plots for PS and %EE (Fig. 2a and b) showed strong linear agreement, with data points clustering tightly near the regression line, proving the predictive ability of the model. Canonical analysis of the response surface (Fig. 2c) revealed a saddle point for PS and a maximum for %EE, signifying complex and opposing interactions between total lipid and Tween-80 concentrations.

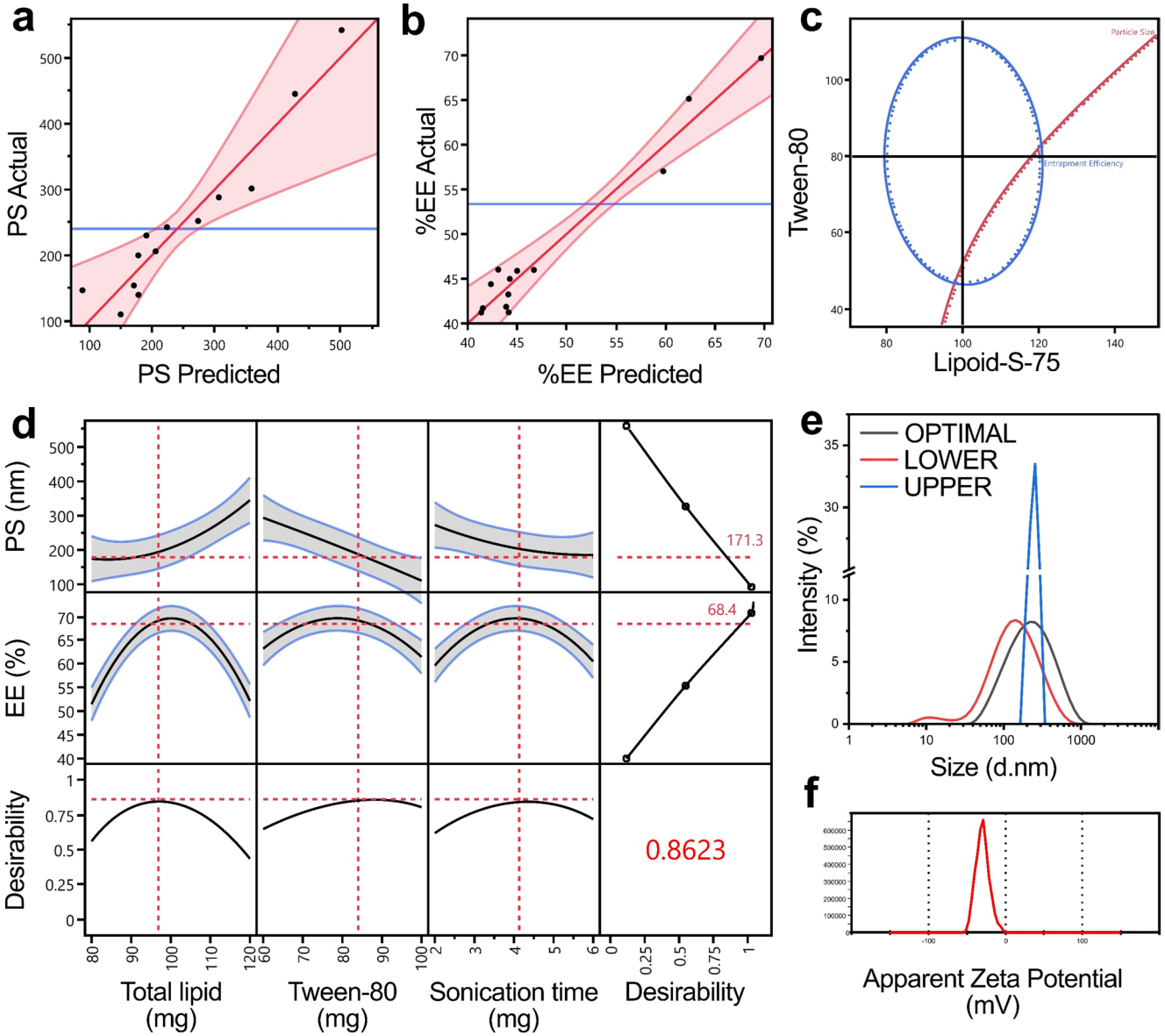

Fig. 2 Optimisation and model validation for BA-NPs. (**a–b**) Predicted vs. observed PS and %EE. (**c**) Overlay contour plot defining design space. (**d**) Desirability function illustrating optimal conditions in the form of prediction profilers. (**e–f**) DLS-based PS distribution and ζ-potential of optimised formulation

In Fig. 2d, the prediction profiler graphically represents the influence of each factor on the responses. It was observed that increasing the total lipid and Tween-80 concentrations led to larger PS, which is likely due to the enhanced lipid thickness and the formation of concentric structures. On the opposite side, %EE decreased at higher levels of these lipids, potentially due to saturation of the lipid matrix. Sonication time exhibited a parabolic relationship with both responses. Initial increases led to a reduction in PS due to improved dispersion, but excessive sonication may disrupt particle integrity.

A comprehensive desirability-based optimisation was performed to simultaneously optimise both CQAs. The optimal batch (Fig. 2d) was identified at a total lipid concentration of 98.36 mg (1:1 ratio of Lipoid-S-75 to RO), 86.08 mg of Tween-80, and a sonication time of 4.09 min. This combination predicted a particle size of 169.90 nm and an EE of 68.35%, achieving a high composite desirability score of 0.8625, indicating a strong model fit.

Further validation of the optimal formulation was conducted through PS analysis and %EE assessment. The PS and PDI were found to be approximately 174 ± 2.1 nm and 0.25, respectively, as shown in Fig. 2e, thereby confirming the validity of the model. The formulation exhibited a %EE of 67.5 ± 1.2% and a drug loading of 3.53 ± 0.5%. Zeta potential analysis (Fig. 2f) revealed a surface charge of approximately − 30.01 mV, indicating adequate colloidal stability. Finally, statistical modelling and desirability-based optimisation successfully identified a robust design space for the BA-NP system.

3.4 Characterisation of Baicalin-loaded Nano Lipidic Particles

The primary physiological characterisation of BA-NPs revealed that the formulation displays desirable nanoscale properties for effective topical delivery. The PS of the optimised BA-NPs was measured to be 174 ± 2.1 nm, falling well within the nanoscale range that improves enhanced permeation into deeper layers of the skin. The surface charge (ζ-potential) was approximately − 30.01 mV, suggesting sufficient electrostatic repulsion to maintain colloidal stability and prevent particle aggregation.

%EE of BA-NPs, determined via the centrifugation method, was found to be 67.5 ± 1.2%, indicating efficient drug entrapment within the nanocarrier matrix. Morphological evaluation using AFM and TEM further supported these findings. AFM images (Fig. 3c) demonstrated a spherical morphology with a topographic height ranging between ~ 150–200 nm, while TEM analysis (Fig. 3d) confirmed smooth and spherical structures with uniform distribution of BA-NPs, but with a larger size, which may be due to aggregation in the machine vacuum.

These preliminary results indicate successful nanoparticle formulation. In the following subsections, advanced characterisation techniques are discussed to provide a comprehensive evaluation of the developed BA-NP system.

3.4.1 Fourier Transform Infrared (FTIR) Spectroscopy

As shown in Fig. 4f, pure BA characteristic peaks are marked in green, including broad –OH stretching around ~ 3400 cm^{-1} and C = O stretching near 1650 cm^{-1} [57]. These peaks were preserved in the physical mixture (PM), with some minor shifts, indicating no significant chemical interaction among components. In BA-NPs spectra, the intensity of characteristic peaks was markedly reduced and broadened, particularly in the –OH and C = O regions, suggesting successful encapsulation of BA within BA-NPs. The absence of sharp, distinctive peaks corresponding to unformulated BA further confirmed its incorporation into the nanolipid structure.

3.4.2 Powder X-ray Diffraction

In Fig. 4c, BA exhibited sharp, high-intensity peaks at 2θ angles of 8.53°, 10.28°, 12.36°, 14.63°, 20.58°, 25.35°, and 27.98°, confirming its highly ordered crystalline nature. In contrast, the BA-NPs showed peaks with significantly lower intensity, indicating loss of crystallinity. This reduction in diffraction intensity confirms the successful encapsulation of BA within the nanocarrier matrix and shows its transformation to a less crystalline state, which may enhance solubility and bioavailability.

3.4.3 Drug Release and Model Fitting

The release profiles at pH 5.2 and 7.4 were selected to reflect the acidic microenvironment of psoriatic lesions and the neutral conditions of deeper viable skin layers. Although psoriatic skin typically exhibits a surface pH of ~ 5.5, localised inflammation can further lower the pH, making a pH of 5.2 a relevant model that mimics a disease-associated condition. The drug release behaviour of BA solution and BA-NPs was assessed, and it was found that BA solution exhibited a rapid and complete release within 6–7 h under both conditions. In contrast, BA-NPs showed a sustained and pH-dependent release (Fig. 4a). At pH 5.2, complete release occurred over 36 h, whereas at pH 7.4, only ~ 52% of the drug was released in the same period. This suggests that BA-NPs remain intact under neutral pH and preferentially release the drug in acidic environments, relevant for targeted

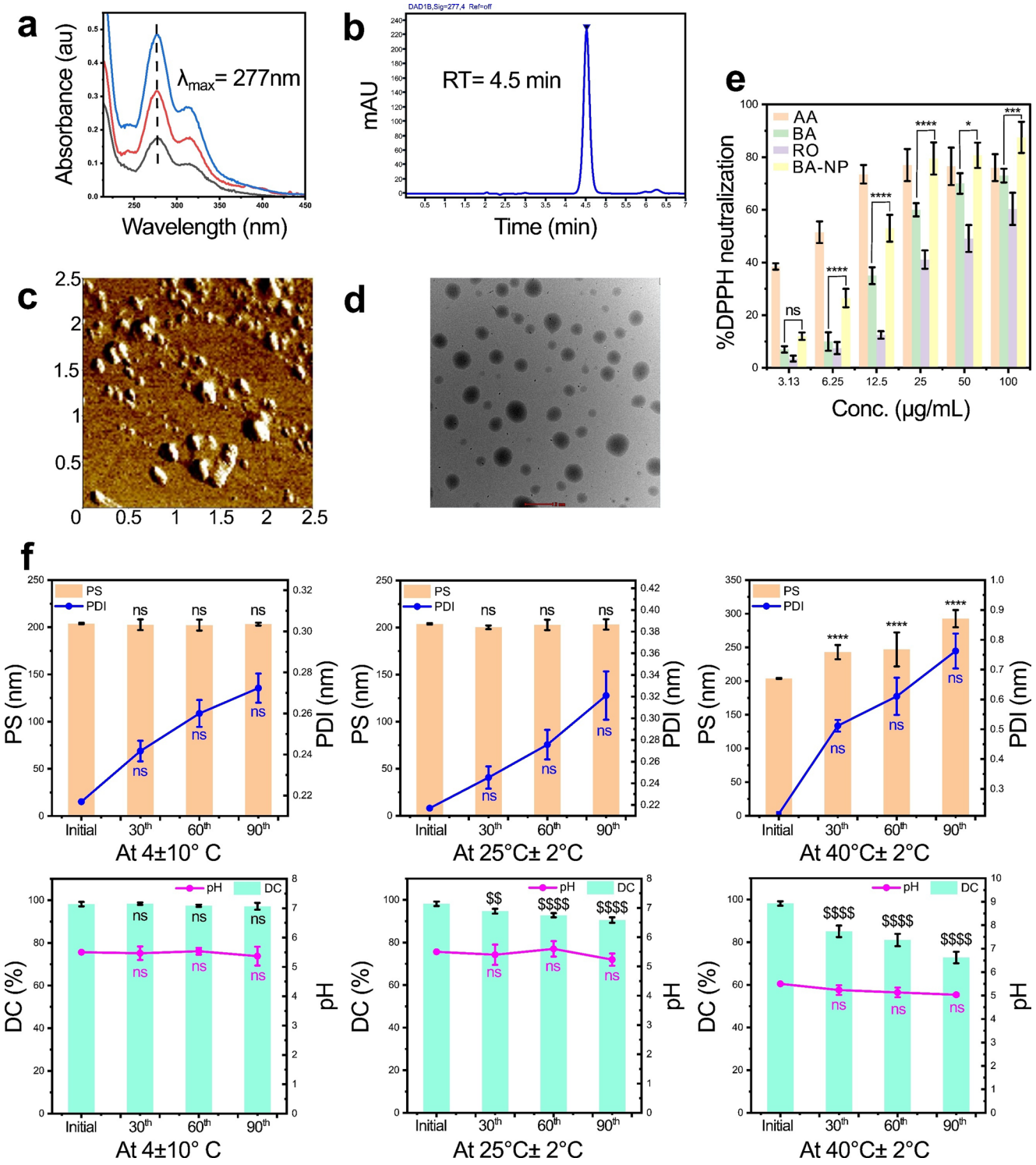

Fig. 3 Physicochemical and antioxidant activity evaluation. (**a**) UV spectrum of BA; (**b**) Chromatogram confirming purity of BA via HPLC; (**c–d**) Surface morphology analysis using AFM (Unit of scale is µm) and TEM (Scale = 2 µm) imaging; (**e**) DPPH assay evaluating antioxidant activities (Two-way ANOVA followed by Tukey's test: ****$p < 0.0001$, ***$p = 0.0005$, *$p = 0.0143$, ns > 0.05 vs. BA-NPs); (**f**) 3-month stability assessment showing PS ($p < 0.0001$), PDI (ns), drug content ($$$p = 0.0044$, $$$$$p < 0.0001$, ns), and pH (ns) relative to initial readings (data analysed using two-way ANOVA with Tukey's multiple comparison test)

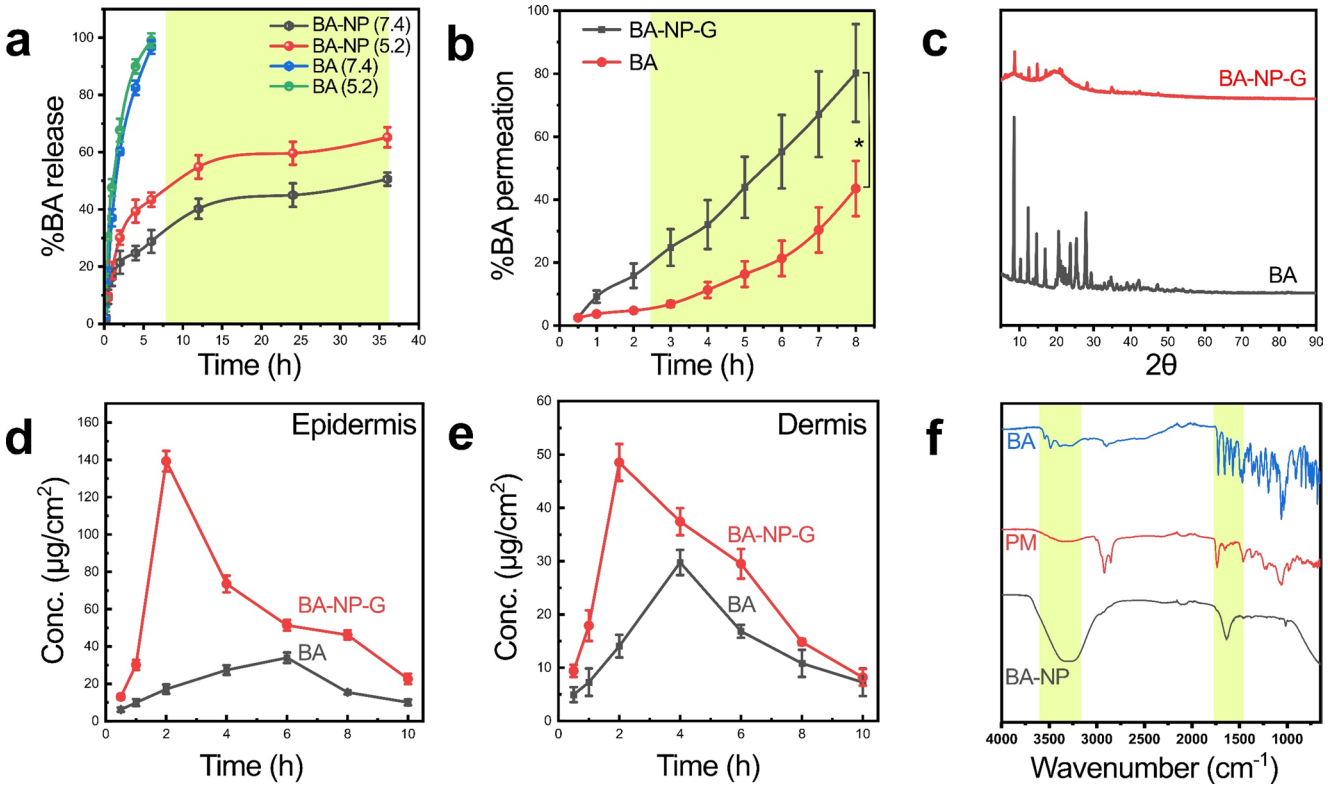

Fig. 4 Characterisation (**a**) In vitro drug release profile at pH 5.2 and 7.4; (**b**) Comparative skin permeation (data analysed using paired Student's *t*-test, $p = 0.0304$); (**c**) XRD graphs showing crystallinity; (**d–e**) Drug deposition in epidermis and dermis; (**g**) FTIR spectra confirming formulation compatibility

delivery in inflammatory tissues. Kinetic modelling further supported this behaviour. At pH 5.2, the release data fit best with the Korsmeyer–Peppas model, yielding an adjusted R^2 of 0.9085, an AIC of 55.58, and an MSC of 2.08, confirming an excellent model fit. The model predicted a diffusion-controlled mechanism, consistent with the observed sustained release, thereby validating the formulation's potential for controlled and site-responsive drug delivery.

3.5 Cytoprotective, Anti-Inflammatory, and Antioxidant Effect of BA-NPs in LPS-Stimulated RAW264.7 Macrophages

The cytocompatibility of BA, BA-NPs, and blank nanoparticles (B-Ns) was evaluated in RAW264.7 macrophages. As shown in Fig. 5a, both BA and BA-NPs exhibited concentration-independent cell viability, maintaining more than 85% survival across the entire range tested (1.56–100 µg/mL). This shows a less cytotoxic effect in macrophages under the experimental conditions. Although BA-NPs overall showed slightly higher cell viability compared to bulk BA; the differences were not statistically significant, suggesting that nano formulation did not introduce any additional cytotoxicity.

Importantly, B-Ns showed nearly 100% cell viability, confirming its excellent cytocompatibility and serving as a biologically safe drug delivery carrier. These results showed the suitability of BA-NPs for further cell response assays.

3.5.1 LPS-induced Cellular Inflammation

Exposure of LPS (1 µg/mL) to RAW264.7 macrophages showed a time-dependent cytotoxic effect (Fig. 5c). At 12 and 24 h, cells are viable, maintaining high (above 90%) viability across all tested concentrations (0.25–1 µg/mL), indicating minimal early-stage cytotoxicity. However, at 48 h, a significant reduction in viability was observed, specifically at 1 µg/mL LPS, decreasing to approximately 60% compared to the 12-hour reading ($p < 0.0001$), while the lower concentrations remained non-cytotoxic. Statistical analysis revealed no significant difference between 12 h and 24 h; however, a highly significant decrease occurred at 48 h, reflecting the progression of LPS-induced inflammatory injury. Based on these results, 1 µg/mL LPS at 24-hour exposure was selected for further cell response studies.

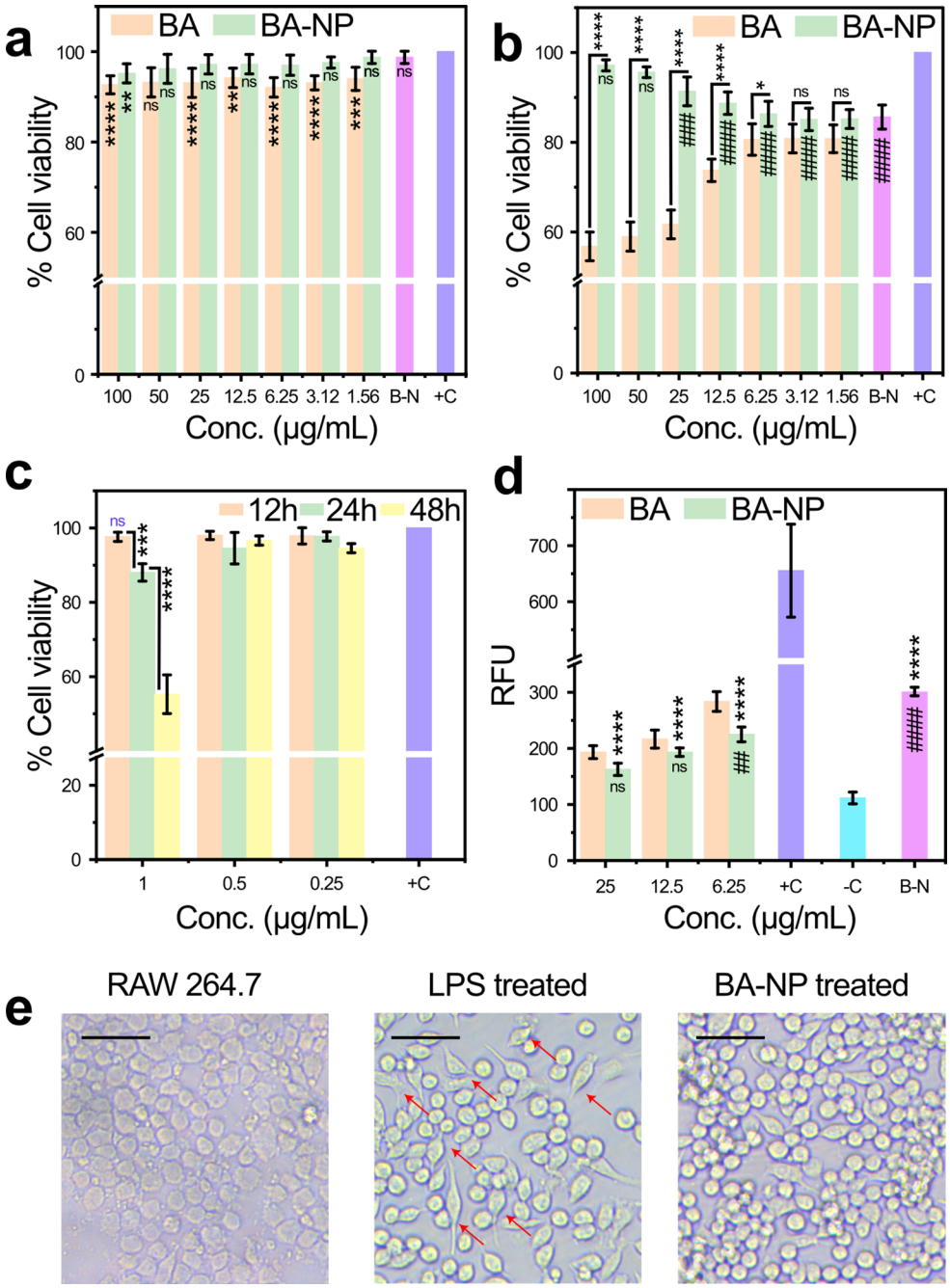

Fig. 5 (**a**) Cytotoxicity in RAW 264.7 cells comparing BA and BA-NPs (Two-way ANOVA followed by Tukey's test, ****p < 0.0001, ***p = 0.0001, **p = 0.0019 vs +ve control); (**b**) Cell viability after LPS induction and treatment (Two-way ANOVA followed by Tukey's test: ****p < 0.0001, *p = 0.0236 for BA vs BA-NP, and ####p < 0.0001, ###p = 0.0002, ns vs +ve control); (**c**) Cytotoxicity post LPS challenge (Two-way ANOVA followed by Tukey's test, 12h vs 24h:***p = 0.0002; 24h vs 48h: p < 0.0001); (**d**) ROS quantification (Two-way ANOVA followed by Tukey's test, ##p = 0.0090, ####p < 0.0001, ns vs -ve control); (**e**) Morphological changes before and after treatment in activated macrophages

3.5.2 Treatment of BA, BA-NPs, and B-Ns in LPS-Stimulated Cells

As shown in Fig. 5b, treatment with BA, BA-NPs, or B-Ns showed a significant concentration-dependent restoration of viability. In the treatment groups, BA-NPs demonstrated the most robust cytoprotective response, specifically at concentrations of 25–100 µg/mL, where cell viability increased above 90%. BA-NPs maintained statistically superior viability compared to free BA at concentrations of 100, 50, 25 and 12.5 µg/mL (****$p < 0.0001$), and remained moderately but significantly better even at 6.25 µg/mL (*$p < 0.05$), suggesting enhanced cellular internalisation due to nanoparticle-mediated delivery and controlled release of the active compound. Interestingly, B-Ns treatment restored cell viability to ~90%, suggesting a therapeutic role of RO, possibly due to its anti-inflammatory and antioxidant properties.

3.5.3 ROS Modulation

In Fig. 6a, it is clearly visible that RAW264.7 macrophages exposed to LPS (+C or Positive control) exhibit intense

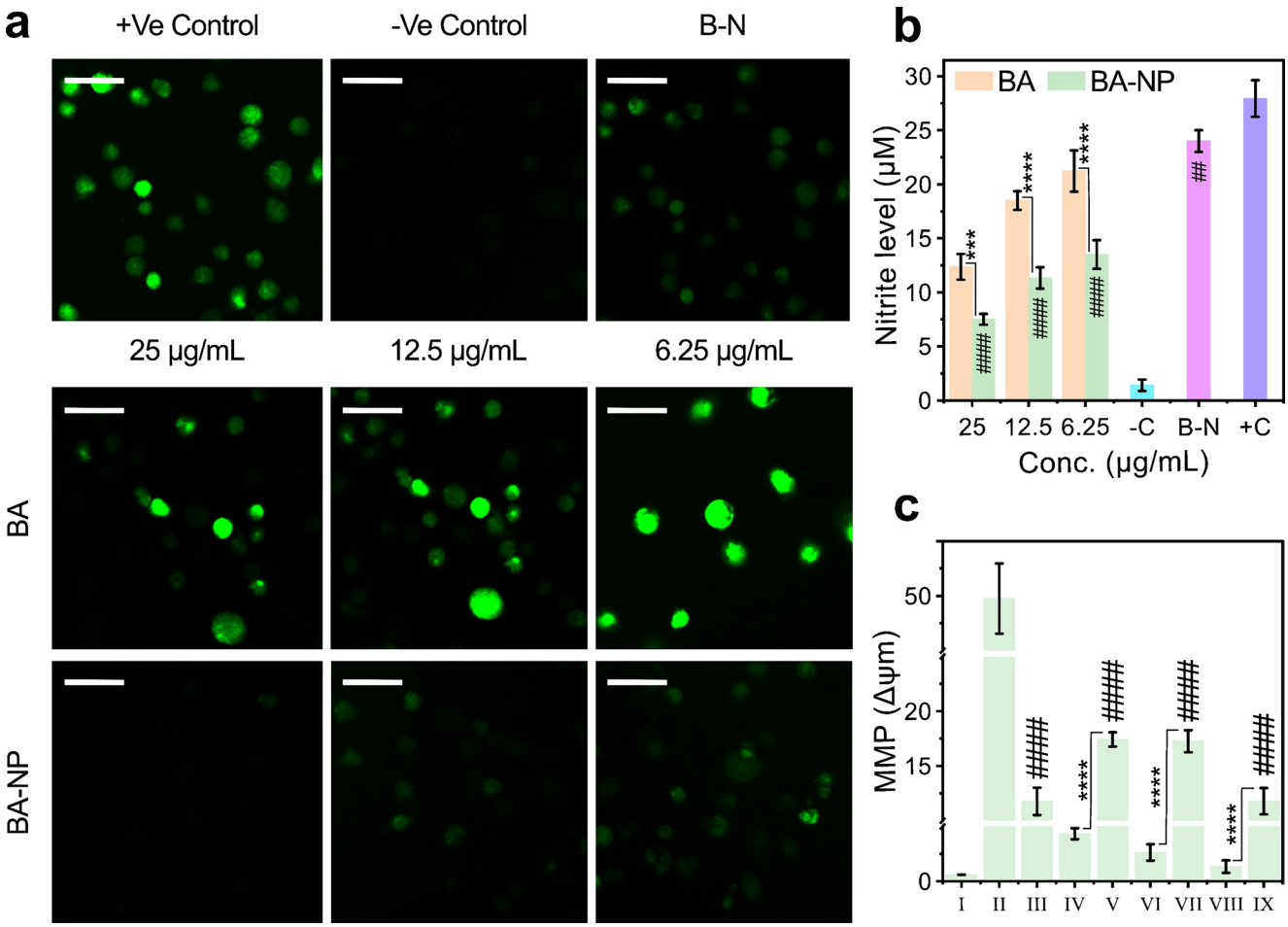

Fig. 6 Evaluation of intracellular stress and inflammatory markers. (**a**) Fluorescent detection of ROS using DCFDA assay (scale = 500 µm); (**b**) Nitrate production levels (Two-way ANOVA followed by Tukey's test, ***$p = 0.0002$, ****$p < 0.0001$ for BA vs. BA-NPs; ##$p = 0.0029$, ####$p < 0.0001$ vs. +ve control); (**c**) Mitochondrial membrane potential evaluation (One-way ANOVA followed by Tukey's test, ####$p < 0.0001$ for LPS vs. BA-NPs and B-Ns; ****$p < 0.0001$ for BA vs. BA-NPs)

green fluorescence, indicating high intracellular ROS levels. In contrast, the untreated control group (–C or Negative control) showed minimal fluorescence, confirming baseline oxidative homeostasis. Within the treated groups, BA gave a moderate reduction in ROS levels, suggesting partial antioxidant defence. In comparison, BA-NPs exposure showed a significant attenuation of ROS fluorescence, specifically at 25 µg/mL, where signal intensity was strongly reduced and visually similar to the –C group. This result was further supported by the quantitative DCF-DA assay (Fig. 5d), where BA-NPs at 6.25 and 25 µg/mL showed a significant reduction in ROS levels, bringing them close to those of the healthy control (-C). Interestingly, B-Ns also exhibited notable ROS scavenging activity, as visible decreased fluorescence intensity and a significantly lower RFU compared to the LPS control (****$p < 0.0001$).

3.5.4 Nitrite Levels

A hallmark of inflammatory activation (nitrite levels) via the inducible nitric oxide synthase (iNOS) pathway was evaluated using the Griess assay. As illustrated in Fig. 6b, RAW264.7 macrophages stimulated with LPS (+C or positive control) exhibited high nitrite levels (~30 µM), confirming a strong pro-inflammatory response. In contrast, untreated cells (–C or negative control) exhibited minimal nitrite production (~4 µM), representing the baseline for healthy cells. When LPS-stimulated cells were treated with BA-NPs, it showed superior inhibition at all tested concentrations, with high effect at 25 µg/mL, where nitrite levels were reduced to approximately 9 µM (****$p < 0.0001$ vs. +C). In comparison, BA achieved only moderate NO suppression, with nitrite levels remaining above 12 µM, and

statistically inferior to BA-NPs at corresponding concentrations. B-Ns also induced nitrite level reduction (~20 µM), significantly lower than the LPS control (###$p<0.001$), indicating a partial inhibition of NO release.

3.5.5 JC-1 Assay

Mitochondrial membrane potential (ΔΨm), an indicator of mitochondrial health, was assessed using JC-1 staining and fluorescence imaging (Supplementary **Fig. S1**). Healthy untreated cells (Group II) exhibited strong red fluorescence due to JC-1 aggregates, indicating an intact mitochondrial membrane. In contrast, LPS-stimulated cells (Group I) exhibited a significant decrease in red fluorescence, accompanied by an increase in green fluorescence, indicating mitochondrial depolarisation caused by inflammation. Upon treatment with BA and BA-NPs, a significant restoration of ΔΨm was observed in a dose-dependent manner. Specifically, BA-NPs-treated groups (Groups 5, 7, and 9 corresponding to 25, 12.5, and 6.25 µg/mL, respectively) showed a significant improvement in mitochondrial membrane potential when compared to BA only (Fig. 6c). At the highest tested concentration (25 µg/mL), BA-NPs restored ΔΨm to levels making 75–80% close to the healthy cells (****$p<0.0001$ vs. LPS; ###$p<0.001$ vs. corresponding BA group). BA-NPs maintained superior mitochondrial integrity over free BA, indicating more effective protection against LPS-induced mitochondrial collapse. Interestingly, B-Ns (Group 3) also elicited significant recovery of ΔΨm (~60–65% of control, ###$p<0.001$ vs. LPS), underscoring the inherent protective effects of RO.

3.5.6 Morphological Restoration by Treatments

Cell morphology, as observed under phase contrast microscopy (Fig. 5e), revealed profound changes upon LPS exposure. Cells from –C group maintained a round, resting morphology, whereas LPS-treated (+C or positive control) cells exhibited irregular elongation, cellular spreading, and pseudopodia formation (marked in red)—typical markers of inflammation. Upon treatment with BA-NPs, cells largely retained their native morphology, similar to that of untreated controls, indicating suppression of LPS-induced morphological changes.

3.6 Gel Rheological Behaviour

The BA-NPs was successfully incorporated into different concentrations of Carbopol and xanthan gum gel and evaluated for its rheological behaviour. As shown in Fig. 7a, all formulations have shear-thinning (non-Newtonian pseudoplastic) behaviour, which is a highly desirable property for topical gels. Specifically, the 0.75% BA-NP-G demonstrated a nearly uniform viscosity across varying shear rates, showing closer alignment to the marketed anti-psoriatic hydrogel and superior consistency compared to the corresponding blank gel. This suggests stable structural integrity at rest and ease of spreadability during application. The pseudoplastic character of 0.75% BA-NP-G was further confirmed by the shear stress versus shear rate curve (Fig. 7b), which shows a nonlinear rise in shear stress, indicative of a well-developed internal network structure that resists deformation under stress and rapidly recovers after application.

Fig. 7 Rheological and texture profile of BA-NP-G. (**a–d**) non-Newtonian flow behaviour under varied shear conditions; (**e–h**) Amplitude, frequency, and strain sweep confirming viscoelastic and mechanical integrity; (**i**) Texture profile illustrating consistency and spreadability

Time-dependent viscosity studies (Fig. 7c) revealed moderate thixotropic properties of the 0.75% BA-NP-G, characterised by a minimal viscosity drop over time and greater kinetic stability compared to its blank gel, while approaching the performance of the MF. Additionally, the temperature-dependent viscosity profile (Fig. 7d) illustrated that the formulation retained consistent viscosity across a broad thermal range (20–50 °C), affirming its thermal resilience and suitability under variable storage conditions. Collectively, data from Fig. 7a and d strongly support the selection of 0.75% BA-NP-G as the optimised formulation.

In amplitude sweep analysis (Fig. 7e), the blank gel, BA-NP-G, and MF all displayed a wide linear viscoelastic region (LVER), indicating network stability under low oscillatory stress. However, BA-NP-G showed a pronounced increase in storage modulus (G′), indicating superior elastic character and suggesting an enhanced rigidity of the gel network—a crucial factor for maintaining shape and stability during storage and use. Frequency sweep studies (Fig. 7f) further validated the viscoelastic profile; both G′ and G″ remained relatively stable across varying angular frequencies. This frequency independence signifies a robust internal matrix. Notably, BA-NP-G demonstrated consistently higher G′ values than marketed formulation (MF), and the incorporation of BA-NPs did not adversely impact the rheological spectrum, confirming homogeneous integration within the gel matrix and excellent mechanical integrity.

The deformation response of the gel was evaluated via shear stress versus strain (Fig. 7g), which revealed a nonlinear increase in strain with increasing stress, characteristic of pseudoplastic materials. Such a profile is favourable for topical use, ensuring that the gel retains its structure under static conditions while becoming sufficiently fluid upon mechanical manipulation, facilitating smooth application and spreadability. Furthermore, analysis of complex viscosity against angular frequency (Fig. 7h) showed that BA-NP-G possessed higher viscosity than MF and exhibited a

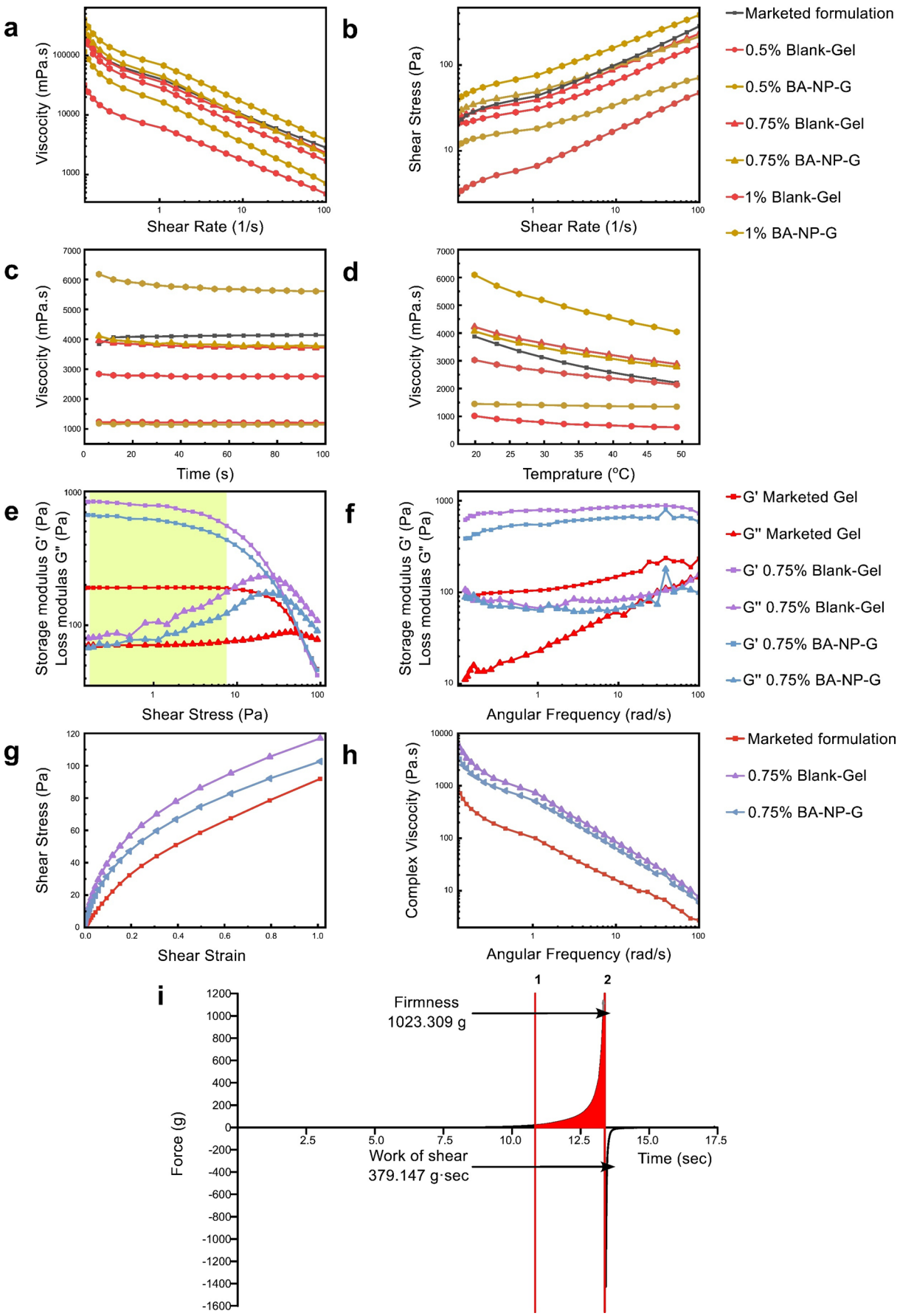
a
Viscocity (mPa.s)
Shear Rate (1/s)
b
Shear Stress (Pa)
Shear Rate (1/s)
Marketed formulation
0.5% Blank-Gel
0.5% BA-NP-G
0.75% Blank-Gel
0.75% BA-NP-G
1% Blank-Gel
1% BA-NP-G
c
Viscocity (mPa.s)
Time (s)
d
Viscocity (mPa.s)
Temprature (°C)
e
Storage modulus G' (Pa)
Loss modulas G" (Pa)
Shear Stress (Pa)
f
Storage modulus G' (Pa)
Loss modulas G" (Pa)
Angular Frequency (rad/s)
G' Marketed Gel
G" Marketed Gel
G' 0.75% Blank-Gel
G" 0.75% Blank-Gel
G' 0.75% BA-NP-G
G" 0.75% BA-NP-G
g
Shear Stress (Pa)
Shear Strain
h
Complex Viscocity (Pa.s)
Angular Frequency (rad/s)
Marketed formulation
0.75% Blank-Gel
0.75% BA-NP-G
i
Force (g)
Firmness
1023.309 g
Work of shear
379.147 g·sec
Time (sec)
1
2

decreasing trend with increasing frequency, reiterating its shear-thinning behaviour. Elevated viscosity also implies enhanced mucoadhesive strength, which is advantageous for prolonged residence time on the skin.

Texture profile analysis (Fig. 7d) revealed that BA-NP-G had a firmness value of 1023.309 g and a work of shear of 379.147 g·s, indicating moderate hardness and a balanced energy requirement for application. These findings suggest that the gel maintains sufficient rigidity while remaining easy to spread.

In addition to rheological robustness, BA-NP-G showed excellent physical and sensory attributes. The organoleptic assessment confirmed that the formulation was soft, white in appearance, non-greasy, odourless, and free from grittiness or phase separation, indicating physical stability. Manual assessment by finger compression showed a smooth, uniform texture. Washability testing demonstrated ease of removal, which may enhance patient compliance. The formulation's pH ranged from 5.0 to 5.5, aligning well with the physiological pH of the skin, ensuring minimal irritation. Drug content analysis performed on samples taken from different depths (top, middle, and bottom) confirmed uniform distribution of the active within the gel matrix, indicating excellent homogeneity.

3.7 Ex Vivo Skin Permeation

BA from the BA-NP-G and BA solutions skin permeation capacity was assessed using Franz diffusion cells over an 8-hour period, as illustrated in Fig. 4b. The BA-NP-G demonstrated a significantly enhanced permeation capacity, achieving closer to 95% cumulative permeation, whereas the BA solution showed only 50% during the same period. This nearly 2-fold increase in permeation is a sign of superior dermal delivery potential conferred by the nanocarrier system. The improved performance of BA-NP-G is attributed to the nanoparticulate nature of BA-NPs, which enhances the drug's deeper penetration into skin layers. The gel matrix may act as a sustained-release reservoir, providing a constant and prolonged release of the active compound, in contrast to the BA solution, which lacks this structural advantage and therefore exhibits limited permeation.

Further, quantitative parameters proved the superiority of the gel formulation. The steady-state flux of BA-NP-G was found to be 6.06 µg/cm²/h, compared to 3.64 µg/cm²/h for the BA solution. Correspondingly, the permeability coefficient was also markedly improved in BA-NP-G (0.00303 cm/h) relative to the solution (0.00182 cm/h), suggesting a stronger driving force for drug diffusion from the gel matrix.

3.8 Ex vivo Dermatokinetic Studies

Comparative dermatokinetic evaluation was done to assess the skin distribution dynamics of BA from the BA-Solution and BA-NP-G. The study aimed to characterise and contrast the extent of drug retention in both the epidermal and dermal layers, which are therapeutically relevant skin layers for managing chronic inflammatory skin diseases such as psoriasis. The findings are graphically represented in Fig. 4d–e and quantitatively summarised in Table 3.

3.9 Stability and Shelf-Life Estimation

Stability studies of intermediate as well as final product were conducted to examine the effect of different storage conditions (4 ± 1 °C, 25 ± 2 °C, and 40 ± 2 °C) on the physical and chemical properties of the formulation over 3 months (Fig. 3f). At 4 ± 1 °C, there were no significant changes in PS or PDI of BA-NPs over time ($p > 0.05$, ns), and the DC remained above 95% with stable pH values in the case of BA-NP-G. At 25 ± 2 °C, visible increase in PS and PDI was seen by day 90 (PS: ****$p < 0.0001$; PDI: ####$p < 0.0001$), along with a gradual reduction in DC (significant by day 60 and 90, \$\$$p < 0.01$, \$\$\$$p < 0.001$, \$\$\$\$$p < 0.0001$), while pH values showed minor fluctuations. At 40 ± 2 °C, PS and PDI increased significantly at all intervals (PS: **$p < 0.0001$; PDI: ####$p < 0.0001$), and DC declined significantly at all points beyond the initial value ($p < 0.0001$), while the pH remained relatively unchanged (ns, $p > 0.05$).

Extrapolation of stability data, as illustrated in Supplementary Fig. S-2, using Microsoft Excel, demonstrated that samples stored at 4 °C can potentially maintain over 90% drug content for more than 364 days. These findings indicate optimal stability at 4 °C, with higher temperatures accelerating particle destabilisation and drug degradation.

Table 3 Dermatokinetic data of BA-Solution vs. BA-NP-G

	BA-Solution (Dermis)	BA-NP-G (Dermis)	BA-Solution (Epidermis)	BA-NP-G (Epidermis)
$T_{skinmax}$ (h)	4	2	6	2
$C_{skinmax}$ (µg/cm^2)	29.76 ± 2.36	48.52 ± 3.47	33.94 ± 2.79	139.26 ± 5.5
AUC $_{0-t}$	151.11 ± 20.65	262.58 ± 21.31	199.76 ± 19.94	602.52 ± 33.48
Ke	0.22 ± 0.07	0.32 ± 0.024	0.31 ± 0.02	0.21 ± 0.01

4 Discussion

The plant-derived flavonoid BA, identified by its polyphenolic structure, has well-known antioxidant and anti-inflammatory properties. However, its clinical utility is limited due to its poor aqueous solubility and restricted permeability [9, 10]. This study target to address these pharmacokinetic and physicochemical limitations by using the properties of RO and incorporating BA into a nanocarrier system. The developed BA-loaded nanoparticles were further embedded into a Carbopol and xanthan gum matrix, forming BA-NP-G, a composite formulation designed by RO to enhance therapeutic efficacy and facilitate targeted cutaneous delivery. The results demonstrated a synergistic antioxidant and anti-inflammatory effect of BA and RO, with mechanistic evidence at the molecular level supporting their combined action.

The BA-NPs was strategically designed in accordance with the QbD paradigm. Regression analysis with high correlation coefficients (R^2) and minimal residual errors, finding the total lipid and surfactant concentrations as CMAs, while sonication time was found as a CPP. XRD analysis revealed a loss of BA crystallinity upon encapsulation, indicating molecular-level mixing within the lipid matrix. In addition, ATR-FTIR spectroscopy revealed shifts in O–H and C = O stretching vibrations, suggesting the formation of hydrogen bonds and hydrophobic interactions between BA and the lipid components, which are important for stabilising BA within the nanoparticle core. The incorporation of nanoparticles into the hydrogel matrix improved the rheological performance, with the resulting BA-NP-G exhibiting pseudoplastic, shear-thinning behaviour—an advantageous property for topical formulations.

Ex vivo skin permeation and dermatokinetic studies confirmed improved deposition of BA within deeper skin layers following application of BA-NP-G. The nano-size and structural robustness of BA-NPs likely facilitated transcellular transport, possibly by passing through tight junctions and promoting lipid membrane fusion. The hydrogel component functioned as a depot system, maintaining a controlled local concentration gradient. The low Ke and elevated AUC values suggest efficient accumulation of BA in the skin, a salient feature for therapeutic management of chronic skin conditions like psoriasis.

Compared to bulk BA, the BA-NPs significantly enhanced free radical scavenging activity, as demonstrated by lower IC_{50} values in DPPH assays. This improved efficacy may be attributed to the high surface area and reduced molecular mobility within the BA-NPs, resulting in a higher local concentration of active BA at the interface. In RAW 264.7 cells, intracellular ROS levels were lowered following BA-NPs treatment, as visible in decreased fluorescence in the DCFDA assay. These results suggest that BA-NPs minimises oxidative stress, possibly through preservation of the glutathione (GSH) pool and inhibition of NADPH oxidase. It is also possible that BA-NPs activates the Nrf2–Keap1 pathway, thereby increasing antioxidant enzymes such as superoxide dismutase (SOD) and catalase, as evidenced by sustained ROS suppression over time.

Further, BA-NPs reduced LPS-induced nitrite production and restored cell viability in macrophages, likely via suppression of inducible nitric oxide synthase (iNOS) (Fig. 1a). Interestingly, even B-Ns showed therapeutic potential, possibly due to the intrinsic bioactivity of RO present in B-Ns as an excipient. The anti-inflammatory effects are believed to be mediated through inhibition of the Toll-like receptor 4 (TLR4)/MyD88 signalling pathway, which is activated by LPS and further transduced through the nuclear factor kappa B (NF-κB) and mitogen-activated protein kinase (MAPK) cascades [34, 58, 59]. At the molecular level, BA is known to suppress phosphorylation of ERK1/2, JNK, and p38 MAPK, thereby interfering with the expression of inflammatory mediators [60]. Nanoencapsulation of BA likely prolongs intracellular retention and sustains these anti-inflammatory effects. Finally, JC-1 staining assays confirmed that BA-NP-G restores mitochondrial membrane potential ($\Delta\psi m$), a crucial parameter in maintaining ATP synthesis and overall mitochondrial function.

5 Conclusion

This research presents the preliminary development and characterisation of BA-NP-G as a prototype formulation intended for the management of psoriasis. A QbD approach was employed to systematically evaluate the influence of formulation components and process parameters, achieving favourable preliminary characteristics for the BA-NPs. This provides a scientific basis for further optimisation and scale-up of the formulation in subsequent studies. The developed BA-NPs exhibited nanometric size, high entrapment efficiency, and sustained drug release for up to 8 h when incorporated into a hydrogel matrix. Ex vivo dermatokinetic analysis confirmed deeper accumulation and improved skin retention of BA, showing the system's potential for targeted therapeutic action. Further, LPS-stimulated RAW 264.7 cell response studies showed that the formulation significantly reduced oxidative stress and inflammation. These effects are primarily due to the pharmacological activity of BA, while RO, employed as a bioactive excipient, contributed to synergistic antioxidant and skin-penetrating properties. Together, these findings underscore the BA-NPs potential as a targeted and synergistic approach for treating inflammatory skin conditions.

Supplementary Information The online version contains supplementary material available at https://doi.org/10.1007/s12668-025-02337-z.

Acknowledgements The authors acknowledge the Department of Pharmaceuticals, Ministry of Chemicals and Fertilisers, Government of India, for financial support and express their gratitude to the CoE-NDDS NIPER-Raebareli for its valuable support. The NIPER-R communication number for the research article is NIPER-R/Communication/818.

Author Contributions ADS: Conceptualisation, Data curation, Experimentation, Writing- original draft. KKS: Writing- Review & editing RS: Conceptualisation, Writing- Review & editing, Supervision.

Funding None.

Data Availability Data will be made available on request.

Declarations

Competing interests The authors declare no competing interests.

Animal Ethics All animal experiments were conducted in accordance with the guidelines of the Committee for the Purpose of Control and Supervision of Experiments on Animals (CPCSEA), Government of India. The experimental protocol was reviewed and approved by the Institutional Animal Ethics Committee (IAEC) of the National Institute of Pharmaceutical Education and Research (NIPER), Raebareli, under approval number NIPER/RBL/IAEC/228/SEP.2024.

References

1. Raharja, A., Mahil, S. K., & Barker, J. N. (2021). Psoriasis: A brief overview. *Clinical Medicine*, *21*(3), 170–173. https://doi.org/10.7861/clinmed.2021-0257
2. Sieminska, I., Pieniawska, M., & Grzywa, T. M. (2024). The immunology of psoriasis—Current concepts in pathogenesis. *Clinical Reviews in Allergy & Immunology, 66*(2), 164–191. https://doi.org/10.1007/s12016-024-08991-7
3. Kim, W. B., Jerome, D., & Yeung, J. (2017). Diagnosis and management of psoriasis. *Canadian Family Physician Medecin De Famille Canadien, 63*(4), 278–285.
4. Dobrică, E. C., Cozma, M. A., Găman, M. A., Voiculescu, V. M., & Găman, A. M. (2022). The involvement of oxidative stress in psoriasis: A systematic review. *Antioxidants*, *11*(2), 282. https://doi.org/10.3390/antiox11020282
5. Sutar, A. D., & Shukla, R. (2025). Emerging smart microneedle technologies in psoriasis: Convergence of nanocarriers, machine learning, and personalized delivery. *RSC Pharmaceutics*. https://doi.org/10.1039/D5PM00173K
6. Lee, H. J., & Kim, M. (2023). Challenges and future trends in the treatment of psoriasis. *International Journal of Molecular Sciences*, *24*(17), 13313. https://doi.org/10.3390/ijms241713313
7. Kumar, S., & Shukla, R. (2024). Advancements in microneedle technology: Current status and next-generation innovations. *Journal of Microencapsulation*, *41*(8), 782–803. https://doi.org/10.1080/02652048.2024.2418613
8. Momtaz, E., & Mehrgardi, M. A. (2025). Electro-responsive paper patch for enhanced transdermal methotrexate delivery in psoriasis treatment. *International Journal of Pharmaceutics*, *684*, 126099. https://doi.org/10.1016/j.ijpharm.2025.126099
9. Bao, M., Ma, Y., Liang, M., Sun, X., Ju, X., Yong, Y., & Liu, X. (2022). Research progress on pharmacological effects and new dosage forms of Baicalin. *Veterinary Medicine and Science, 8*(6), 2773–2784. https://doi.org/10.1002/vms3.960
10. Wen, Y., Wang, Y., Zhao, C., Zhao, B., & Wang, J. (2023). The pharmacological efficacy of Baicalin in inflammatory diseases. *International Journal of Molecular Sciences, 24*(11), 9317. https://doi.org/10.3390/ijms24119317
11. Li, Y., Song, K., Zhang, H., Yuan, M., An, N., Wei, Y., & Gao, Y. (2020). Anti-inflammatory and immunomodulatory effects of Baicalin in cerebrovascular and neurological disorders. *Brain Research Bulletin, 164*, 314–324. https://doi.org/10.1016/j.brainresbull.2020.08.016
12. Fadnis, A., Mhaske, A., & Shukla, R. (2025). Neuroprotective potential of Baicalin nanocrystals: Optimisation, comprehensive in vitro SH-SY5Y cell studies and in vivo pharmacokinetics. *BioNanoScience, 15*(2), Article 228. https://doi.org/10.1007/s12668-025-01834-5
13. Durmaz, L., Karagecili, H., & Gulcin, İ. (2023). Evaluation of carbonic anhydrase, acetylcholinesterase, butyrylcholinesterase, and α-glycosidase inhibition effects and antioxidant activity of Baicalin hydrate. *Life, 13*(11), 2136. https://doi.org/10.3390/life13112136
14. Bajek-Bil, A., Chmiel, M., Włoch, A., & Stompor-Gorący, M. (2023). Baicalin—Current trends in detection methods and health-promoting properties. *Pharmaceuticals, 16*(4), 570. https://doi.org/10.3390/ph16040570
15. Yang, J., Li, M., Zhang, C., & Liu, D. (2021). Pharmacological properties of Baicalin on liver diseases: A narrative review. *Pharmacological Reports*, *73*(5), 1230–1239. https://doi.org/10.1007/s43440-021-00227-1
16. Riadi, Y., Afzal, O., Geesi, M. H., Almalki, W. H., & Singh, T. (2023). Baicalin-loaded lipid-polymer hybrid nanoparticles inhibiting the proliferation of human colon cancer: Pharmacokinetics and in vivo evaluation. *Polymers*. https://doi.org/10.3390/polym15030598
17. Sohail, S., Arshad, S., Khalid, S., Dar, M. J., Iqbal, K., & Sohail, H. (2023). Development and evaluation of methotrexate and Baicalin loaded nano- lipid carriers for psoriasis treatment. *Turkish Journal of Pharmaceutical Sciences, 0*(0), 0–0. https://doi.org/10.4274/tjps.galenos.2023.71242
18. Liu, X., Shu, W., Zhong, Q., Zeng, A., Zeng, Y., Gu, H., Chen, P., & Li, X. (2025). A Baicalin liposome-based temperature-sensitive hydrogel for treating ultraviolet-induced skin damage. *International Journal of Nanomedicine, 20*, 7935–7951. https://doi.org/10.2147/IJN.S516572
19. Singh, P. K., Singh, N., Chopra, R., Garg, M., Chand, M., Dhiman, A., & Talwar, B. (2025). Rosemary bioactives as antioxidant agent: A bidirectional approach to improving human health and vegetable oil stability. *Food Chemistry Advances*, *7*, 100952. https://doi.org/10.1016/j.focha.2025.100952
20. Hoseini, S. M., Shakib, P., Ahmadipour, S., & Mohammadi, M. (2025). Formulation, antimicrobial, and antioxidant effect of

anti-acne serum containing extracts of *striata scrophularia* and rosemary plants. *Letters in Drug Design & Discovery,* , Article 100081. https://doi.org/10.1016/j.lddd.2025.100081
21. Vasdev, N., Handa, M., Kesharwani, P., & Shukla, R. (2022). Rosemary oil low energy nanoemulsion: Optimization, μrheology, *in silico, in vitro, and ex vivo* characterization. *Journal of Biomaterials Science, Polymer Edition, 33*(15), 1901–1923. https://doi.org/10.1080/09205063.2022.2088527
22. Ni, H., Wu, Z., Muhammad, I., Lu, Z., & Li, J. (2018). Optimization of Baicalin water extraction process from *scutellaria baicalensis* (a traditional Chinese medicine) by using orthogonal test and HPLC. *Revista Brasileira de Farmacognosia, 28*(2), 151–155. https://doi.org/10.1016/j.bjp.2018.02.001
23. Behera, M., Mahale, P., Gowtham, A., Sutar, A. D., Kaundal, R. K., & Shukla, R. (2025). Quality by design based hydrogel formulation of 4-Octyl itaconate-loaded nanostructured lipid carriers for epidermal restoration in atopic dermatitis. *Journal of Pharmaceutical Investigation*. https://doi.org/10.1007/s40005-025-00748-4
24. Angeli, L., Morozova, K., & Scampicchio, M. (2023). A kinetic-based stopped-flow DPPH• method. *Scientific Reports*, *13*(1), 7621. https://doi.org/10.1038/s41598-023-34382-7
25. Shahgaldian, P., Da Silva, E., Coleman, A. W., Rather, B., & Zaworotko, M. J. (2003). Para-acyl-calix-arene based solid lipid nanoparticles (SLNs): A detailed study of Preparation and stability parameters. *International Journal of Pharmaceutics*, *253*(1–2), 23–38. https://doi.org/10.1016/S0378-5173(02)00639-7
26. Sutar, A. D., Verma, R. K., & Shukla, R. (2024). Quality by design in pulmonary drug delivery: A review on dry powder inhaler development, nanotherapy approaches, and regulatory considerations. *AAPS PharmSciTech, 25*(6), Article 178. https://doi.org/10.1208/s12249-024-02900-z
27. Kitao, K., Tani, M., Yamane, M., Inui, S., Yamada, M., & Norisuye, T. (2024). Nano and submicron particle sizing in concentrated suspension by dynamic ultrasound scattering method. *Colloids and Surfaces A: Physicochemical and Engineering Aspects*, *690*, 133807. https://doi.org/10.1016/j.colsurfa.2024.133807
28. Kouchakzadeh, H., Shojaosadati, S. A., & Shokri, F. (2014). Efficient loading and entrapment of Tamoxifen in human serum albumin based nanoparticulate delivery system by a modified desolvation technique. *Chemical Engineering Research and Design*, *92*(9), 1681–1692. https://doi.org/10.1016/j.cherd.2013.11.024
29. Gujrati, A., Khanal, S. R., Pastewka, L., & Jacobs, T. D. B. (2018). Combining TEM, AFM, and profilometry for quantitative topography characterization across all scales. *ACS Applied Materials & Interfaces*, *10*(34), 29169–29178. https://doi.org/10.1021/acsami.8b09899
30. Mathure, D., Sutar, A. D., Ranpise, H., Pawar, A., & Awasthi, R. (2023). Preparation and optimization of liposome containing thermosensitive *In Situ* nasal hydrogel system for brain delivery of Sumatriptan Succinate. *Assay and Drug Development Technologies, 21*(1), 3–16. https://doi.org/10.1089/adt.2022.088
31. Holder, C. F., & Schaak, R. E. (2019). Tutorial on powder X-ray diffraction for characterizing nanoscale materials. *ACS Nano, 13*(7), 7359–7365. https://doi.org/10.1021/acsnano.9b05157
32. Gonsalves, A., Tambe, P., Le, D., Thakore, D., Wadajkar, A. S., Yang, J., & Menon, J. U. (2021). Synthesis and characterization of a novel pH-responsive drug-releasing nanocomposite hydrogel for skin cancer therapy and wound healing. *Journal of Materials Chemistry B*, *9*(46), 9533–9546. https://doi.org/10.1039/D1TB01934A
33. Zhang, Y., Huo, M., Zhou, J., Zou, A., Li, W., Yao, C., & Xie, S. (2010). DDSolver: An add-in program for modeling and comparison of drug dissolution profiles. *AAPS Journal, 12*(3), 263–271. https://doi.org/10.1208/s12248-010-9185-1
34. Tian, Y., Zhou, S., Takeda, R., Okazaki, K., Sekita, M., & Sakamoto, K. (2021). Anti-inflammatory activities of amber extract in lipopolysaccharide-induced RAW 264.7 macrophages. *Biomedicine & Pharmacotherapy*, *141*, 111854. https://doi.org/10.1016/j.biopha.2021.111854
35. Han, S., Gao, H., Chen, S., Wang, Q., Li, X., Du, L. J., & Yang, S. (2019). Procyanidin A1 alleviates inflammatory response induced by LPS through NF-κB, MAPK, and Nrf2/HO-1 pathways in RAW264.7 cells. *Scientific Reports*, *9*(1), 15087. https://doi.org/10.1038/s41598-019-51614-x
36. Mao, Z., Liu, Z., Chen, L., Yang, J., Zhao, B., Jung, Y. M., & Zhao, C. (2013). Predictive value of the surface-enhanced resonance raman scattering-based MTT assay: A rapid and ultrasensitive method for cell viability in situ. *Analytical Chemistry, 85*(15), 7361–7368. https://doi.org/10.1021/ac401254s
37. Xu, J., Chen, H., Qian, H., Wang, F., & Xu, Y. (2022). Advances in the modulation of ROS and transdermal administration for anti-psoriatic nanotherapies. *Journal of Nanobiotechnology*, *20*(1), 448. https://doi.org/10.1186/s12951-022-01651-y
38. Ferrer, M. D., Reynés, C., Jiménez, L., Malagraba, G., Monserrat-Mesquida, M., Bouzas, C., & Pons, A. (2024). Nitrite attenuates the in vitro inflammatory response of immune cells to the SARS-CoV-2 S protein without interfering in the antioxidant enzyme activation. *International Journal of Molecular Sciences*. https://doi.org/10.3390/ijms25053001
39. Giustarini, D., Rossi, R., Milzani, A., & Dalle-Donne, I. (2008). Nitrite and Nitrate Measurement by Griess Reagent in Human Plasma: Evaluation of Interferences and Standardization (pp. 361–380). https://doi.org/10.1016/S0076-6879(07)00823-3
40. Wu, J., Liu, S., Zhang, H., Zhang, X., Xue, J., Li, Z., & Zhao, L. (2025). Amlexanox ameliorates imiquimod-induced psoriasis-like dermatitis by inhibiting Th17 cells and the NF-κB signal pathway. *Biomedicine & Pharmacotherapy*, *184*, 117922. https://doi.org/10.1016/j.biopha.2025.117922
41. Elefantova, K., Lakatos, B., Kubickova, J., Sulova, Z., & Breier, A. (2018). Detection of the mitochondrial membrane potential by the cationic dye JC-1 in L1210 cells with massive overexpression of the plasma membrane ABCB1 drug transporter. *International Journal of Molecular Sciences*, *19*(7), 1985. https://doi.org/10.3390/ijms19071985
42. Shah, A., & Dobrovolskaia, M. A. (2024). Detection of Nanoparticle-Mediated change in mitochondrial membrane potential in T cells using JC-1 dye (pp. 153–159). https://doi.org/10.1007/978-1-0716-3786-9_16
43. Milanović, M., Ćirin, D., & Krstonošić, V. (2021). The interactions in ternary system made of xanthan gum, carbopol 940 and anionic/nonionic surfactant. *Journal of Molecular Liquids, 344*, 117696. https://doi.org/10.1016/j.molliq.2021.117696
44. Gowri, K., & Abdul Rahim, A. (2024). Investigation on rheological performance of indigenously developed sustainable low clinker hybrid cementing binders. *Results in Engineering, 24*, 103543. https://doi.org/10.1016/j.rineng.2024.103543
45. Malana, M. A., Zohra, R., & Khan, M. S. (2012). Rheological characterization of novel physically crosslinked terpolymeric hydrogels at different temperatures. *Korea-Australia Rheology Journal*, *24*(3), 155–162. https://doi.org/10.1007/s13367-012-0019-9
46. Sun, M., Sun, H., Wang, Y., Sánchez-Soto, M., & Schiraldi, D. (2018). The relation between the rheological properties of gels and the mechanical properties of their corresponding aerogels. *Gels*, *4*(2), 33. https://doi.org/10.3390/gels4020033
47. Kokol, V., Pottathara, Y. B., Mihelčič, M., & Perše, L. S. (2021). Rheological properties of gelatine hydrogels affected by flow- and

horizontally-induced cooling rates during 3D cryo-printing. *Colloids and Surfaces A: Physicochemical and Engineering Aspects*, *616*, 126356. https://doi.org/10.1016/j.colsurfa.2021.126356
48. Rogiers, V. (2001). EEMCO guidance for the assessment of transepidermal water loss in cosmetic sciences. *Skin Pharmacology and Physiology*, *14*(2), 117–128. https://doi.org/10.1159/000056341
49. Sekkat, N., Kalia, Y. N., & Guy, R. H. (2002). Biophysical study of Porcine ear skin in vitro and its comparison to human skin in vivo. *Journal of Pharmaceutical Sciences*, *91*(11), 2376–2381. https://doi.org/10.1002/jps.10220
50. Van Bocxlaer, K., Gaukel, E., Hauser, D., Park, S. H., Schock, S., Yardley, V., & Wring, S. A. (2018). Topical treatment for cutaneous leishmaniasis: Dermato-pharmacokinetic lead optimization of benzoxaboroles. *Antimicrobial Agents and Chemotherapy*. https://doi.org/10.1128/AAC.02419-17
51. Tomar, Y., Maheshwari, S., Gorantla, S., & Singhvi, G. (2024). Curcumin loaded liquid crystalline nanoparticles for enhanced topical application: Design, characterization, ex vivo and dermatokinetic evaluation. *Journal of Drug Delivery Science and Technology*, *92*, 105391. https://doi.org/10.1016/j.jddst.2024.105391
52. Qadir, A., Aqil, M., Ali, A., Warsi, M. H., Mujeeb, M., Ahmad, F. J., & Beg, S. (2020). Nanostructured lipidic carriers for dual drug delivery in the management of psoriasis: Systematic optimization, dermatokinetic and preclinical evaluation. *Journal of Drug Delivery Science and Technology*, *57*, 101775. https://doi.org/10.1016/j.jddst.2020.101775
53. Rapalli, V. K., Sharma, S., Roy, A., & Singhvi, G. (2021). Design and dermatokinetic evaluation of Apremilast loaded nanostructured lipid carriers embedded gel for topical delivery: A potential approach for improved permeation and prolong skin deposition. *Colloids and Surfaces B: Biointerfaces*, *206*, 111945. https://doi.org/10.1016/j.colsurfb.2021.111945
54. ICH Q8 (R2) Pharmaceutical development - Scientific guideline. (2014). European Medicines Agency. Retrieved from https://www.ema.europa.eu/en/ich-q8-r2-pharmaceutical-development-scientific-guideline
55. International conference on harmonisation of technical requirements for registration of pharmaceuticals for human use ich harmonised tripartite guideline stability testing of new drug substances and products *Q1A(R2)* (2003).
56. Yurtsever, A. G., Ekmekcioglu, A., Muftuoglu, M., Güngör, S., & Erdal, M. S. (2024). Formulation development and evaluation of Fluvastatin loaded transethosomes: Characterization, stability, in vitro dermal penetration, cytotoxicity and antipsoriatic activity studies. *Journal of Drug Delivery Science and Technology*, *91*, 105234. https://doi.org/10.1016/j.jddst.2023.105234
57. Wang, Y., Xiong, C., Wu, Z., Liu, Y., Qiu, Y., Cheng, X., & Zhou, G. (2019). Synthesis, characterization of a Baicalin-Strontium(II) complex and its BSA-binding activity. *ChemistrySelect, 4*(45), 13079–13088. https://doi.org/10.1002/slct.201902739
58. Kim, M., An, J., Shin, S.-A., Moon, S. Y., Kim, M., Choi, S., & Lee, C. S. (2024). Anti-inflammatory effects of TP1 in LPS-induced Raw264.7 macrophages. *Applied Biological Chemistry, 67*(1), Article 16. https://doi.org/10.1186/s13765-024-00873-y
59. El-Melegy, M. G., Eltaher, H. M., Gaballah, A., & El-Kamel, A. H. (2021). Enhanced oral permeability of trans-Resveratrol using nanocochleates for boosting anticancer efficacy; In-vitro and ex-vivo appraisal. *European Journal of Pharmaceutics and Biopharmaceutics, 168*, 166–183. https://doi.org/10.1016/j.ejpb.2021.08.020
60. Jiang, C., Zhang, J., Xie, H., Guan, H., Li, R., Chen, C., & Zhang, W. (2022). Baicalein suppresses lipopolysaccharide-induced acute lung injury by regulating Drp1-dependent mitochondrial fission of macrophages. *Biomedicine & Pharmacotherapy*, *145*, 112408. https://doi.org/10.1016/j.biopha.2021.112408